Sol and Gel States in Peptide Hydrogels Visualized by Gd(III)-enhanced Magnetic Resonance Imaging

Mahika Weerasekare,[1] Marc B. Taraban,[2] Xianfeng Shi,[3] Eun-Kee Jeong,[4] Jill Trewhella,[5] Yihua Bruce Yu[2,6]

[1]*Department of Pharmaceutics and Pharmaceutical Chemistry, University of Utah, Salt Lake City, UT 84112*

[2]*Fischell Department of Bioengineering, University of Maryland, College Park, MD 20742*

[3]*Department of Physics, University of Utah, Salt Lake City, UT 84112*

[4]*Department of Radiology, University of Utah, Salt Lake City, UT 84112*

[5]*School of Molecular Bioscience, The University of Sydney, Sydney, NSW 2006, Australia*

[6]*Department of Pharmaceutical Sciences, University of Maryland, Baltimore, MD 21201*

Received 31 December 2010; revised 21 February 2011; accepted 22 February 2011
Published online 7 March 2011 in Wiley Online Library (wileyonlinelibrary.com). DOI 10.1002/bip.21612

ABSTRACT:

The hydrogels assembled from a pair of self-repulsive but mutually attractive decapeptides are visualized by magnetic resonance imaging (MRI). It is found that in the absence of Gd(III)-chelate, gelation has little effect on MRI signal intensity. In the presence of Gd(III)-chelate, gelation leads to significant changes in water relaxation and MR signal intensity. The sol to gel transition is best visualized by T_2-weighted imaging using large echo time with the sol producing a bright spot and the gel producing a dark spot. MRI studies point to high local Gd(III)-chelate concentration. Small-angle X-ray scattering study indicates that this local enrichment of Gd(III)-chelate has two contributing processes: first, the aggregation of peptides into fibers; second, within peptide fibers, Gd(III)-chelate further aggregate into clusters. This work demonstrates that the status of peptide-based hydrogels can be visualized by MRI with the aid of covalently linked Gd(III)-chelates. This result has implications for monitoring peptide scaffolds in vivo. © *2011 Wiley Periodicals, Inc. Biopolymers (Pept Sci) 96: 734-743, 2011.*

Keywords: hydrogels; biomaterials; gadolinium chelate; contrast agents; magnetic resonance imaging; small-angle X-ray scattering

This article was originally published online as an accepted preprint. The "Published Online" date corresponds to the preprint version. You can request a copy of the preprint by emailing the Biopolymers editorial office at biopolymers@wiley.com

INTRODUCTION

Gd(III)-chelates have a long history of broad applications in medical magnetic resonance imaging (MRI) as effective contrast agents by virtue of their ability to change water proton relaxation rates (T_1 and T_2).[1] Gd(III)-chelates can help visualize variations in tissue pH, oxidative state, oxygen content, and the concentration of certain metabolites. Recently, it has been demonstrated that Gd(III)-macromolecular or peptide conjugates are capable to sense the receptor environment and/or tissue pH.[2] Such sensitivity with respect to environment opens the possibilities of using Gd(III)-chelates to trace the fate of engineered biomaterials by means of MRI. Indeed, one of the

Additional Supporting Information may be found in the online version of this article.

Correspondence to: Yihua Bruce Yu; e-mail: byu@rx.umaryland.edu

Contract grant sponsor: National Institutes of Health
Contract grant number: EB004416
Contract grant sponsors: Australian Federation Fellowship
Contract grant sponsors: U. S. Department of Energy
Contract grant number: DE-FG02-05ER64026

challenging tasks in the development of tissue repair scaffolds is how to monitoring them over time noninvasively.

The status of tissue repair scaffolds can be monitored through the relaxivities of water protons.[3] For example, changes in $T_{1\rho}$ images in the presence of iron oxide particles encapsulated into hydrogel scaffolds[4] could be used to monitor the integrity of regenerated articular cartilage. However, T_2 imaging, which appears to be a common technique to analyze soft tissue and cartilage,[5] could not be used in this case for monitoring the status of tissue repair due to the high sensitivity of T_2 to iron oxide. This is because in the presence of iron oxide, T_2 becomes insensitive towards changes in the repair process. However, Gd(III)-enhanced MRI is increasingly used to trace the structural changes in articular cartilage implants.[6] The dGEMRIC (delayed $Gd(DTPA)^{2-}$-enhanced MRI of cartilage)[7] allows one to visualize biomacromolecular networks for cartilage formation. However, the delayed and slow penetration of Gd(III)-chelates into the biopolymer scaffold significantly decreases the applicability of the technique in tissue repair monitoring. These prior results point to the evident need to incorporate Gd(III)-chelates into tissue repair scaffolds for their noninvasive monitoring using MRI.

The most straightforward approach for incorporating Gd(III) into tissue repair scaffolds is to covalently conjugate Gd(III)-chelates to the constituent molecules of the scaffolds. The resulting bulky assemblies would have increased rotational correlation time, τ_r, and much better relaxivities.[8] It has been shown that T_1-relaxivity of the hydrogel formed by self-assembling amphiphilic peptides conjugated to Gd(III)-chelates is significantly higher as compared with the control hydrogel assembled from the same peptide without Gd(III)-chelate.[9] Significant enhancement in T_1-weighted MR imaging has been attained when a Gd(III)-chelate was conjugated to a protein of 264 amino acid residues. The resulting assembly was further cross-linked to form high molecular weight hydrogel scaffold with controlled monomer content, sequence, and chain length.[10]

However, size or molecular weight of Gd(III)-conjugates is only one of several factors affecting their relaxivities. For example, in the case of Gd(III)-chelates conjugated to linear polymers, relaxivities do not improve significantly compared to free Gd(III)-chelates. This is partly due to the flexibility of linear polymers, and partly due to slower water exchange rates in polymer-conjugated Gd(III)-chelates as compared with free Gd(III)-chelates.[11] Aside from molecular weight, the relaxivity of Gd(III)-chelates attached to proteins is known to also depend on the amino acid sequence of proteins.[12] Very high relaxivities were detected when Gd(III)-chelates are conjugated to the surface of nano-diamond particles.[13] Favorable results are also obtained when Gd(III)-chelates are conjugated to rigid dendrimers where the relaxivity is less dependent on water exchange rates.[14] Water exchange rate is another factor that affects relaxivities of Gd(III)-conjugates.[15]

These results suggest that the nuclear magnetic relaxation properties of Gd(III)-chelates are controlled not only by the size or molecular weight of Gd(III)-conjugates, but also by the structural characteristics of the assembly, such as the accessibility of the Gd(III) ion to water molecules as well as local distribution of Gd(III)-chelates. Indeed, T_1-relaxivity is known to be controlled by the accessibility of Gd(III)-chelates by water molecules, while T_2-relaxivity strongly depends on the local concentration of Gd(III)-chelates.[1] Most Gd(III)-conjugates that are currently employed as MRI contrast agents demonstrate T_1-dominated relaxation enhancement. However, in cases where local gadolinium concentration is high, such as incorporating 9-12 Gd(III)-chelate into one dextran aggregate,[16] or as in gadolinium oxide nanoparticles,[17] T_2-relaxation enhancement is more than T_1-relaxation enhancement, and the resulting material becomes a T_2-contrast agent. These prior studies suggest that Gd(III)-chelates in sol and gel states might behave differently, thereby generating a MR contrast that can be used to monitor sol to gel transition. We explore this possibility in this work.

In an effort to create peptide-based biomaterials, we designed mutually attractive but self-repulsive oligopeptide pairs. Dissolved in physiological buffers, each peptide exists as a stable solution. Upon mixing, the two peptides assemble into fibrous networks.[18,19] In light of the potential in vivo applications of this type of mixing-induced hydrogels, it would be very valuable if the two states of hydrogel, sol and gel, show a sharp contrast in MR images so that the status of the hydrogel can be monitored by MRI. In this work, we conducted MR imaging studies of the sol and gel states with and without Gd(III)-chelate. It was found that only in the presence of Gd(III)-chelate can a sharp contrast between sol and gel be produced. Structure of the hydrogel, with and without Gd(III)-chelate, is probed by small-angle X-ray scattering (SAXS) technique.

MATERIALS AND METHODS

Peptide Synthesis and Purification

The chemical structures of the two free peptides (**1** and **2**) and the two paramagnetic chelate-peptide conjugates (**3** and **4**) used in this study are shown in Table I. The negatively charged peptide module, **1**, contains neutral Trp and Ala and negatively charged Glu. The positively charged peptide module, **2**, contains neutral Trp and Ala and positively charged Orn (ornithine). Ornithine is used instead of

Table I Sequences of Oligopeptides and the Structures of Paramagnetic Chelates[a]

Compound No.	Peptide Sequences	M_w (Da)
1	formyl-EFEAEAEAEW-amide	1235.7
2	formyl-OFOAOAOAOW-amide	1162.7
3	[Gd(do3a)]GGGOFOAOAOAOW-amide	1848.0
4	[Eu(do3a)]GGGOFOAOAOAOW-amide	1842.7

Structures of paramagnetic peptide chelates

3

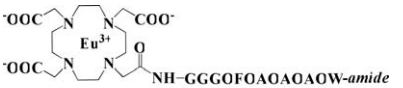

4

[a] Modular material assembly is achieved by pairing a positively charged module (**2**, **3**, and **4**) with a negatively charged module (**1**). A, alanine; E, glutamic acid; F, phenylalanine; G, glycine; O, ornithine; W, tryptophan. do3a refers to the macrocyclic chelator 1,4,7,10-tetraazacyclododecane-1,4,7-triacetic acid. The *C*-terminals of **1**, **2**, **3,** and **4** are amidated (-amide); The *N*-terminal of **1** and **2** are formylated (formyl-).

lysine to increase aqueous solubility (ornithine has one fewer —CH_2— group in its side chain compared to lysine). For the same reason, *N*-terminals of the two gelator peptides, **1** and **2**, were formylated instead of acetylated.[20] To obtain the formylation agent, 2,4,5-trichloro formic acid, dicyclohexyl carbodiimide, and 2,4,5-trichloro phenol were added to a solution of 98% formic acid in ethylacetate precooled to 0°C. The reaction mixture was then filtered and sequentially washed with 150 mL of saturated $NaHCO_3$ aqueous solution and 150 mL of water. The end product was obtained after drying over Na_2SO_4 for 1 hr followed by rotary evaporation ($\sim$96% yield).

Oligopeptides were synthesized using Fmoc solid-phase peptide synthesis method[21] and formylation of the *N*-terminal was carried out using five-fold excess of 2,4,5-trichloro formic acid under ice-cold condition for 1 hr. A ninhydrin test for free *N*-terminal was used to monitor the completion of the formylation reaction. After cleavage from the resin, oligopeptides were purified by ion-exchange and reversed-phase HPLC, using a HP100 preparative chromatography system. The purity of each oligopeptide was verified by analytical HPLC, using a HP100 analytical chromatography system. (See additional Supporting Information.)

For ion-exchange preparative HPLC, a Zorbax strong-anion exchange column (22.5 mm $\times$ 250 mm) was used for purifying the negatively charged **1**; and a Zorbax strong-cation exchange column (22.5 mm $\times$ 250 mm) was used for purifying the positively charged **2**, **3,** and **4**. For reversed-phase preparative HPLC, a ZORBAX C_{18} column (22.5 mm $\times$ 250 mm) was used. For analytical HPLC, a XDB-C_{18} column (4.6 mm $\times$ 250 mm) was used. The eluents for anion-exchange chromatography were A: 10 m*M* NH_4HCO_3 in water, pH 7; B: 2*M* NH_4Cl, 10 m*M* NH_4HCO_3 in 80%MeCN/20%H_2O, pH 7. The eluents for cation-exchange chromatography were A: 0.05% TFA in water, pH 2; B: 2*M* NH_4Cl in 80%MeCN/20%H_2O with 0.05% TFA as the pH modifier. The eluents for reversed-phase HPLC were the same as the ones for ion-exchange chromatography, except that there is no NH_4Cl in eluent B. The flow rate was 5 mL/min for preparative runs and 1 mL/min for analytical runs. The temperature was 25°C in all runs. In all runs, a linear gradient was used (typically 0.25%B/min for preparative runs and 1 or 2%B/min for analytical runs).

The mass value for each oligopeptide was verified by MALDI-MS using Voyager DE-STR (PerSeptive Biosystems/ABI) with 337 nm nitrogen laser, 3 ns pulse, maximum 20 Hz firing rate, operated in a linear detector mode. (See additional Supporting Information.)

Fmoc-Gly-Gly-Gly-COOH (Fmoc-GGG) was synthesized using a known procedure[22] with slight modification: 6.0 g of GGG (31.7 mmol) was added to a solution of 8.4 g of sodium carbonate (79.25 mmol) in water (80 mL) followed by 45 mL of tetrahydrofuran, and the mixture was cooled to 0°C. Then 8.2 g (31.7 mmol) of Fmoc-Cl was added in small portions to the cooled mixture and the resulting mixture was equilibrated to room temperature for 4 hr followed by overnight stirring. The resulting precipitate was dissolved in 800 mL of water and extracted with ethylacetate (3 $\times$ 200 mL). The aqueous fraction was cooled in an ice-water bath, acidified, and refrigerated overnight, then centrifuged to separate a fine precipitate that was then lyophilized to obtain Fmoc-GGG as a white solid (13 g, 31.6 mmol, $\sim$100% yield).

[(do3a)]GGGOFOAOAOAOW-amide was synthesized by adding four-fold excess of Fmoc-GGG to protected and resin-bound **2**. After removing the Fmoc-group by 20% piperidine in dimethyl-formamide, 2.5-fold excess of [(do3a)]-*tris*-(*t*-butyl ester) was added. A longer reaction time (48 hrs) was necessary for conjugating [(do3a)]-*tris*-(*t*-butyl ester) to the *N*-terminus of the resin-bound peptide. After deprotection and cleavage from the resin with 90% trifluoroacetic acid and 2.5% each of ethylene dithiol, tri-isopropyl silane, water, and dichloromethane, the product was concentrated by rotary evaporation, washed with ether, dissolved in water/acetonitrile, and lyophilized. The resulting solid was purified using cation-exchange and reversed-phase preparative HPLC to obtain [(do3a)]GGG-OFOAOAOAOW-amide.

To obtain **3**, [(do3a)]GGGOFOAOAOAOW-amide (86 mg, 0.05 mmol) was dissolved in 1*M* NH_4OAc buffer at pH 7. To this, $GdCl_3$

(26 mg, 0.1016 m*M*) was added and pH of the resulting solution was adjusted to pH 7. After stirring at room temperature for 1 hr, the pH of the solution was increased to 9 to precipitate out excess Gd(III) ions. After filtration the pH was adjusted back to 7. The resulting compound **3** was purified by reversed-phase preparative HPLC at pH 7. Compound **4** was synthesized following the above procedure for compound **3**, and $EuCl_3$ was used instead of $GdCl_3$. Mass values for **3** and **4** were verified using MALDI-MS and their purity was assessed by analytical HPLC.

Peptides were dissolved in 100 m*M* NaCl and 50 m*M* sodium phosphate buffer (phosphate-buffered saline, PBS), pH 7. Samples for MRI experiments were prepared using 70% H_2O + 30% D_2O while samples for SAXS experiments were prepared using 5% H_2O + 95% D_2O. Concentrations of the peptide solutions were determined on the basis of the molar absorptivity of tryptophan at 280 nm ($\varepsilon_{280} = 5690M^{-1}$ cm^{-1})[23] and ICP-OES of Gd(III) or Eu(III) (Perkin-Elmer, Optima 3100XL).

Three hydrogels were prepared from **1**, **2**, **3,** and **4**, including: gel **1** + **2**, which contains no Gd(III)-chelate; gel **1** + **3**, which contains Gd(III)-chelate; and gel **1** + **3/4**, which contains Gd(III)-chelate diluted by Eu(III)-chelate.

Relaxivity Measurements and MRI

Sample Preparation. For all MRI experiments, each compound (**1**, **2**, **3,** and **4**) was dissolved in PBS buffer (70% H_2O + 30% D_2O, pH 7 with no correction for D_2O). For the relaxivity measurements, one phantom was prepared with solutions containing mixtures of **3** and **4**; the concentration of **3** was varied from 0.1 to 1.0 m*M*, while the concentration of **4** was varied correspondingly from 4.9 to 4.0 m*M* to keep the total concentration of **3** and **4** equal to 5 m*M*. In the relaxivity measurements of gel **1** + **3/4**, the concentration of **1** was always 5 m*M* while the concentrations of **3** and **4** were the same as in sol **3/4**. Also, to measure the relaxivity of **4**, its concentration was varied from 0.1 to 2.5 m*M*.

To collect MR images, two phantoms were prepared. The first phantom contained sol **1** (5 m*M*), sol **2** (5 m*M*), gel **1** + **2** (5 m*M* + 5 m*M*), sol **3** (5 m*M*), and gel **1** + **3** (5 m*M* + 5 m*M*). The second phantom contained sol **3/4** (1 m*M*/4 m*M*) and gel **1** + **3/4** (5 m*M* + 1 m*M*/4 m*M*).

Relaxation Measurements and MR Imaging. Relaxivity measurements and T_1- and T_2-weighted images were performed using a Siemens Trio 3 Tesla clinical MRI system (Siemens Medical Solutions, Erlangen, Germany) with Avanto gradients (45 mT/m strength and 150 T/m/s slew rate). The transmit/receive wrist coil was used for the transmission of the RF wave and signal detection to and from the sample. Net magnetization amplitude for each sample was determined from the appropriate region of interest using MRIcro software.[24]

T_1-weighted images were obtained using the inversion-recovery spin echo pulse sequence[25] with a 192 × 256 imaging matrix, 135 × 180 mm^2 field of view, 0.7 × 0.7 mm^2 in-plane resolution with 2.5 m slice thickness, 100 Hz/pixel receiver bandwidth, 5.0 s TR, and 16 ms TE for variable inversion recovery times (TI) of 25, 35, 50, 75, 100, 200, 400, 800, and 1600 ms.

For T_2-weighted imaging, a turbo-spin echo[26] was employed using a 144 × 256 imaging matrix, 100 × 180 mm^2 field of view, 0.7 × 0.7 mm^2 in-plane resolution with 2.5 m slice thickness, 130 Hz/pixel receiver bandwidth, and 3.0 s repetition time (TR). The experiment was repeated for variable echo times (TE) of 12, 24, 35, 47, 59, 71, 83, 94, and 106 ms.

Small-Angle X-ray Scattering (SAXS)

Sample Preparation. 10 mM solutions of **1**, **2,** and **3** were prepared in PBS buffer (5% H_2O + 95% D_2O) and equilibrated on ice. For hydrogel formation, **1** was mixed with equal amount of **2** or **3** gravimetrically so the concentration of each gelator in the mixture is 5 m*M*. The mixture was vortexed in a 1.5 mL centrifuge tube kept on ice to slow down gelation initiation. The mixed sample was immediately centrifuged (30 s at < 2500 rpm) into a 1 mm thin-walled (0.001 mm) glass capillary (Charles Supper Company) fixed in a brass holder (which was also pre-equilibrated on ice) and placed into the sample holder of SAXS instrument, which was thermostated at 12°C (the temperature at which the gelation was monitored).

SAXS Data Measurements and Analysis. SAXS data were acquired at 12°C and reduced to $I(q)$ versus q using the SAXS instrument and procedures described previously.[27] The parameter q is the amplitude of the scattering vector (q-range for our experiments was 0.006–0.32 $Å^{-1}$), and is equal to $4\pi(\sin\theta)/\lambda$, where 2θ is the scattering angle and λ is the wavelength of the incident X-ray (λ = 1.54 Å). The inverse Fourier transform of $I(q)$ gives the pair distance or vector length distribution function, $P(r)$, for the scattering particle and this function is calculated using indirect Fourier transform methods.[28–30] The r value at which $P(r)$ goes to 0 gives the maximum linear dimension for the scattering particle, d_{max}. The second moment of $P(r)$ is the radius of gyration of the scattering particle, R_g.

Guinier analysis for rod-shaped objects was used to analyze elongated fibrils formed as a result of hydrogelation. Guinier showed that when one dimension of the particle is much larger than the other two, the scattering in the small q region (from 0.01 to 0.02 $Å^{-1}$) can be approximated as[31]

$$qI(q) = I_c(0)e^{-q^2R_c^2/2} \quad (1)$$

where R_c is the average radius of gyration of the cross-section of the particle and $I_c(0)$ is proportional to the average mass per unit length along the fiber.

For more detailed modeling of the cross-sectional shape, we used a simulated annealing algorithm implemented in a purpose-written program that is described elsewhere.[32] This algorithm is a 2D implementation of the 3D dummy atom modeling of Svergun.[33] In all calculations, dummy atoms were arranged in a grid with dimensions of 30 × 50 of dummy atoms. Based on the estimates of the resolution of SAXS technique,[34] the reasonable size of each dummy atom was 3 Å in diameter [in order not to affect the results of final model fit, this value should be $< \pi/(2q_{max})$, which is 4.9 Å for our $q_{max} \sim 0.32$ $Å^{-1}$]. The program evaluates pair distance distribution function [$P_c(r)$] for the cross-section of the fibers and calculates the scattering profile of the fibers. From $P_c(r)$, the maximum cross-sectional dimension (D_c), the cross-sectional area (S_c), and the radius of gyration of the cross-section (R_c), were determined. Corrections for the instrument slit geometry, scaling, and incoher-

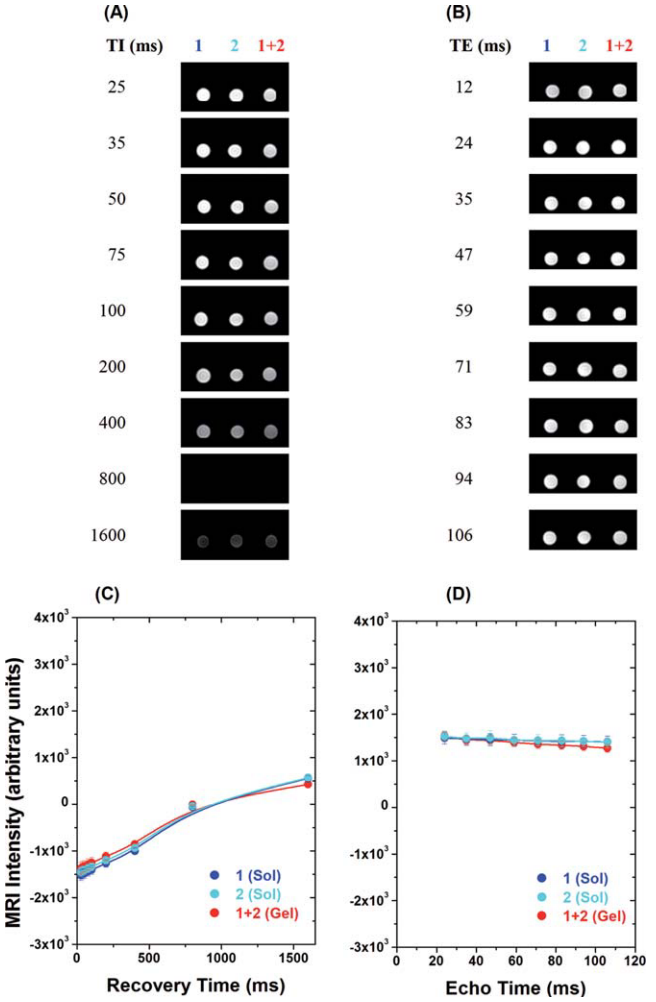

FIGURE 1 Images of hydrogelation with no Gd(III)-chelate. (A) T_1-weighted images with different inversion recovery time TI; (B) T_2-weighted images with different echo time TE; (C) MRI intensity vs. TI; (D) MRI intensity vs. TE.

ent background are applied to compare the simulated model profile with experimental scattering data.[32]

RESULTS AND DISCUSSION

Relaxivity Determination and MRI

Hydrogelation in the Absence of Gd(III)-chelate (Gel 1 + 2). Figure 1 shows that in the absence of Gd(III)-chelate, gelation produced negligible change in MR signal intensity and MR images of gel **1** + **2** are almost identical to those of sol **1** and sol **2**. These results indicate that in the absence of Gd(III)-chelate, there is negligible contrast between the sol and the gel states. This is hardly surprising considering that ~99% w/w of the hydrogel is water. In light of this, we conjugated Gd(III)-chelate to one of the gelator peptides, with the hope that covalently bound Gd(III)-chelate would result in significant MR signal change upon gelation.

Hydrogelation in the Presence of Gd(III)-chelate (Gel 1 + 3). Figure 2 shows that in the presence of covalently bound Gd(III)-chelate, gelation indeed produced drastic change in MR signal intensity, to the point that the gel is completely dark in both T_1- and T_2-weighted images. This is due to complete signal saturation, which makes it impossible to extract T_1 and T_2 values. Such signal saturation suggests high Gd(III) concentration. But the overall Gd(III) concentration in gel **1** + **3** is the same as in sol **3**, which is 5 m*M* in both cases. The fact that the MR signal is not saturated in sol **3** but saturated in gel **1** + **3** points to high local Gd(III) concentration as a result of peptide gelation.

The sharp contrast between sol **3** and gel **1** + **3** means that the gelation process can be visualized using either T_1-weighted imaging at long TI values (Figure 2A) or T_2-weighted imaging

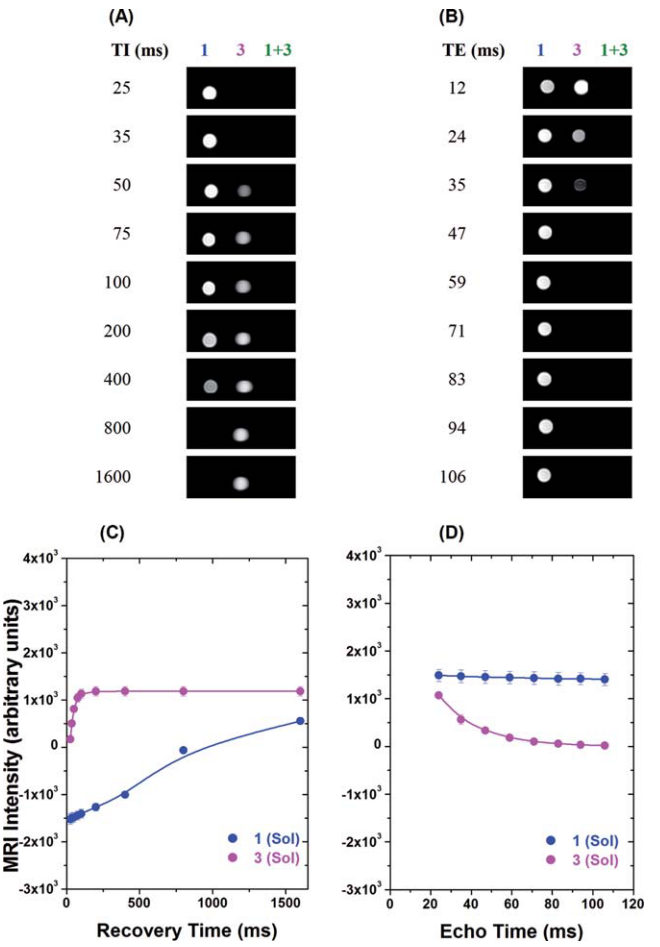

FIGURE 2 Images of hydrogelation with Gd(III)-chelate. (A) T_1-weighted images with different inversion recovery time TI; (B) T_2-weighted images with different echo time TE; (C) MRI intensity vs. TI; (D) MRI intensity vs. TE.

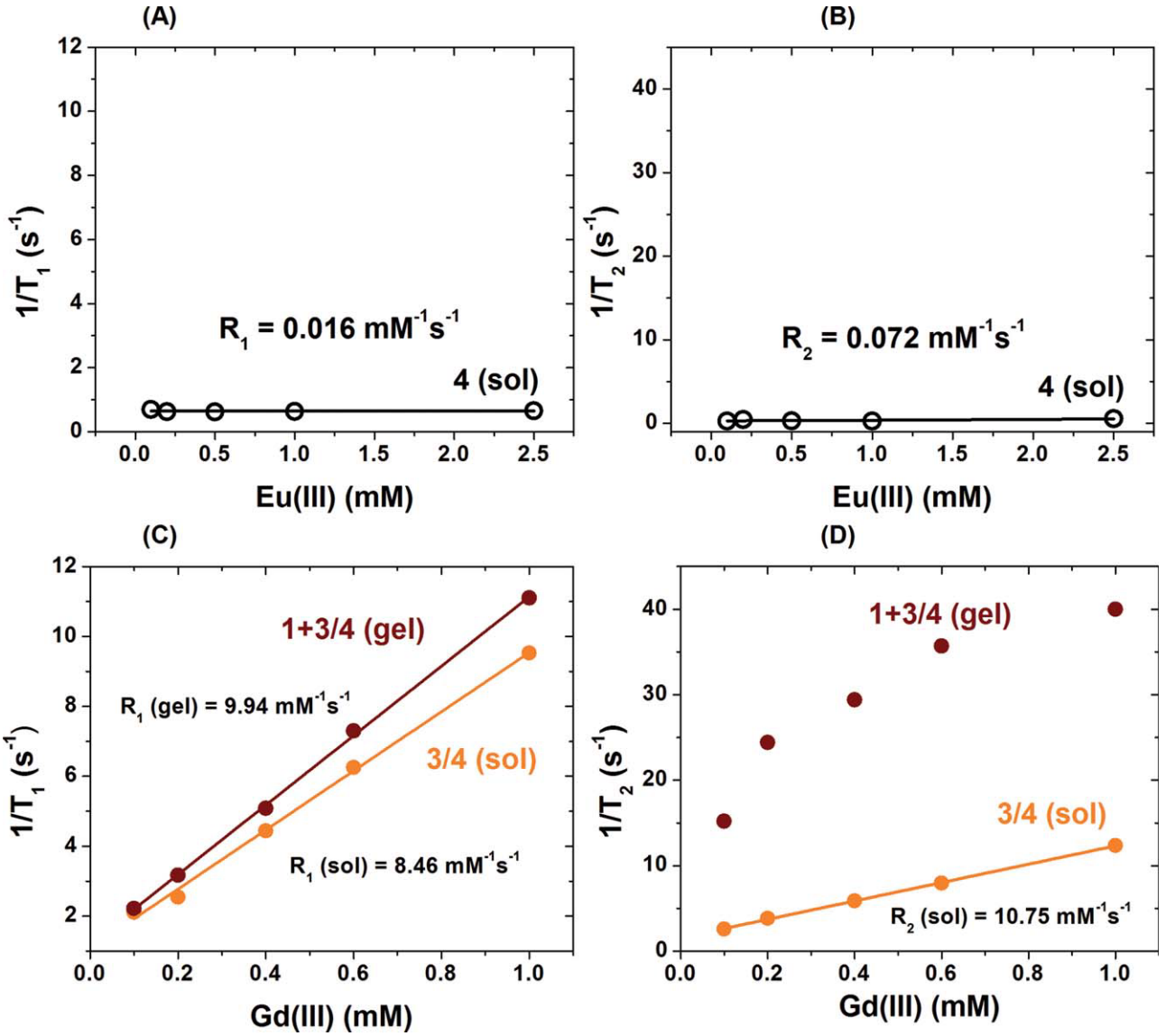

FIGURE 3 T_1 (A) and T_2 (B) in sol **4**. The concentration of **4** was varied from 0.1 to 2.5 m*M*. T_1 (C) and T_2 (D) in sol **3/4** (orange) and in gel **1** + **3/4** (wine). In sol **3/4**, the total concentration of **3** and **4** is 5 m*M* with that of **3** varied from 0.1 to 1.0 m*M*, and that of **4** was varied correspondingly from 4.9 m*M* to 4.0 m*M*. In gel **1** + **3/4**, the concentration of **1** is 5 m*M* while the concentrations of **3** and **4** are the same as in sol **3/4**. The T_1-relaxivity, R_1, and the T_2-relaxivity, R_2, are calculated from the slope of linear fit; the goodness of fit for (A) and (B) is 0.985 and that for (C) and (D) is 0.9995. R_2, was not calculated for gel **1** + **3/4** due to the nonlinearity of the data, which is indicative of clustering of Gd(III)-chelates in the hydrogel matrix.

at short TE values (Figure 2B), with the sol producing bright spots and the gel producing dark spots.

Hydrogelation in the Presence of Diluted Gd(III)-chelate (Gel 1 + 3/4). If the saturation of MR signal in gel **1** + **3** is indeed caused by high local Gd(III)-chelate concentration, then reducing the overall Gd(III)-chelate concentration has the potential to eliminate saturation. However, simply lowering the concentrations of both **1** and **3** from 5 to 1 m*M* will abolish gelation. To solve this difficulty, we opted to "dilute" Gd(III)-chelate by the structurally and chemically similar Eu(III)-chelate. It is well-known that Eu(III)-chelates, the closest analog of Gd(III)-chelates, are much weaker MRI contrast agents as compared to Gd(III)-chelates, and present little influence on the relaxation rates of ^1H_2O. The dilution of Gd(III)-chelate with Eu(III)-chelate is realized by making

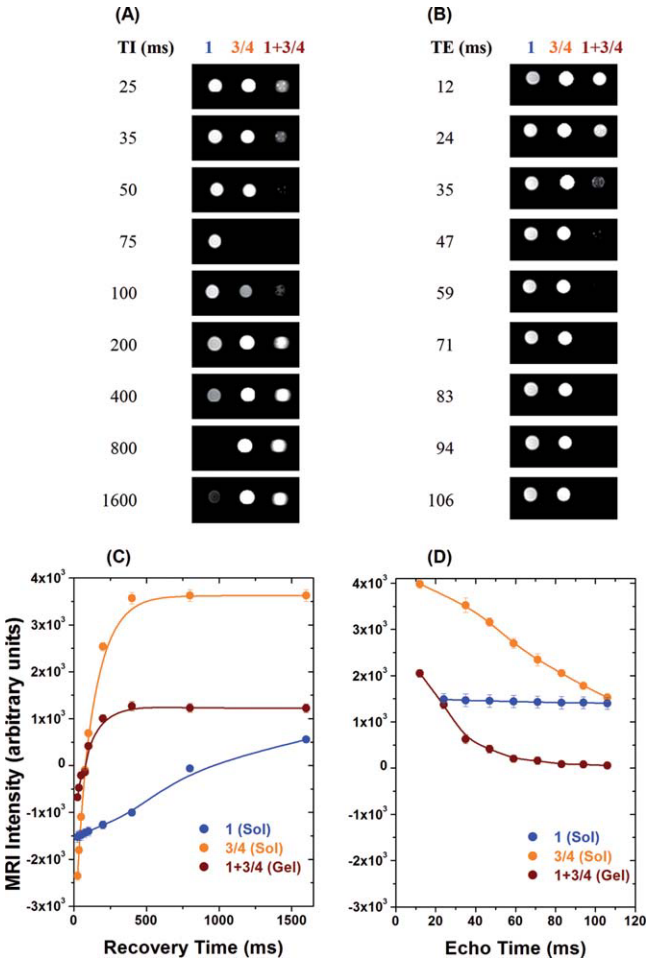

FIGURE 4 Images of hydrogelation with Gd(III)-chelate diluted by Eu(III)-chelate. (A) T_1-weighted images with different inversion recovery time TI; (B) T_2-weighted images with different echo time TE; (C) MRI intensity vs. TI; (D) MRI intensity vs. TE.

a new compound, **4**, in which Eu(III)-chelate is conjugated to the gelator **2** (Table I). Diluting **3** with **4** is far better than diluting **3** with **2** because the structural dissimilarity between **3** and **2** may cause significant structural variation in the resulting hydrogel.

To confirm that **4** indeed has little effect on water relaxation, T_1 and T_2 of ^1H_2O at various concentrations of **4** are determined. As expected, the T_1 and T_2 relaxivities of **4** are 0.016 mM^{-1} s^{-1} and 0.072 mM^{-1} s^{-1}, respectively, much lower than those of **3**, which are 8.46 mM^{-1} s^{-1} and 10.75 mM^{-1} s^{-1}, respectively (Figure 3).

With 1 m*M* overall Gd(III)-chelate, MR signal from gel is no longer saturated. Indeed, gel **1** + **3/4** produced bright spots in MR images at certain TI and TE values (Figure 4), attesting to the effectiveness of diluting **3** with **4**. As for water relaxivity, gelation shortened T_1 only slightly, with the T_1 relaxivity increased from 8.46 mM^{-1} s^{-1} for sol **3/4** to 9.94 mM^{-1} s^{-1} for gel **1** + **3/4** (Figure 3). However, gelation shortened T_2 significantly. Further, unlike T_1, T_2 in gel **1** + **3/4** does not have a linear dependency on Gd(III) concentration, once again suggesting high local concentration of Gd(III)-chelates in the hydrogel.

With T_1 slightly elevated in the gel, one might have expected gel **1** + **3/4** to have higher signal intensity and

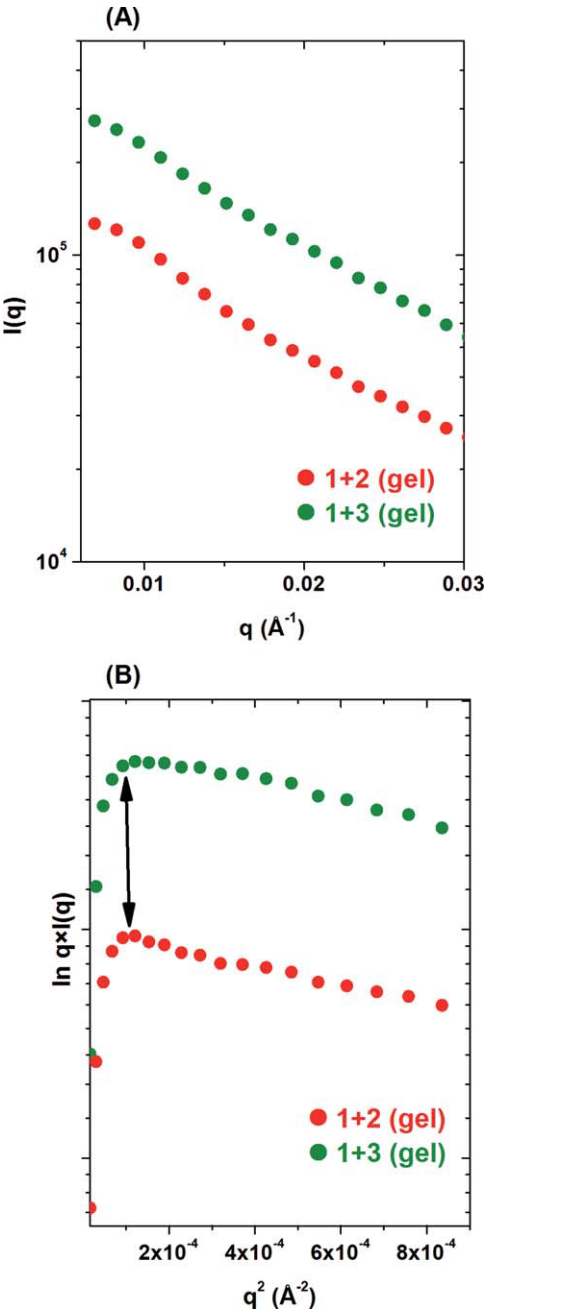

FIGURE 5 Scattering profiles of $I(q)$ vs. q (A) and the corresponding Guinier plots for rod-like particles (B). Scattering data were collected after 24 hr of gelation; red circles, gel **1** + **2**; green circles, gel **1** + **3** pair. Arrows in the Guinier plots mark the roll-over points characteristic for rod-shaped particles.

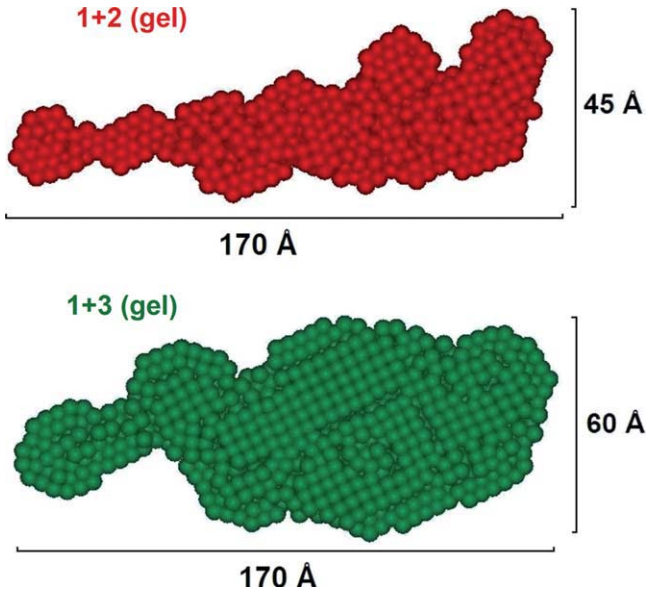

FIGURE 6 Representative 2D dummy atom models of the cross-sections of the fibers in gel **1** + **2** (red) and gel **1** + **3** (green).

thereby brighter spots in T_1-weighted images than sol **3/4**. But the opposite was observed: gel **1** + **3/4** produces lower signal intensity than sol **3/4** (Figure 4C) and less bright spots in T_1-weighted images (Figure 4A). The explanation of this observation lies in the fact that T_2 is shortened to a much greater extent than T_1 upon gelation (Figures 3C and 3D). Keep in mind that MR signal intensity SI is determined not only by T_1 but also by T_2 with the following functional form:

$$\mathrm{SI} \propto \left[1 - 2\exp\left(-\frac{\mathrm{TI}}{\mathrm{T_1}}\right)\right] \times \exp\left(-\frac{\mathrm{TE}}{\mathrm{T_2}}\right) \qquad (2)$$

where TI and TE are the recovery and echo times, respectively.[25,26] It is seen from Eq. (2) that T_1 shortening enhances SI while T_2 shortening reduces SI. When T_2-relaxivity dominates, that is, when T_2 is shortened to a much greater extent than T_1, SI can decrease even as T_1 is shortened. At 1 m*M* Gd(III) upon gelation, T_1 has a 15% reduction, from 104.8 ms in sol **3/4** to 89.8 ms in gel **1** + **3/4** while T_2 has a 70% reduction, from 81.2 ms in sol **3/4** to 25.0 ms in gel **1** + **3/4**. Clearly, as a result of aggregation of Gd(III) in the gel, T_2 relaxation dominates, which is reflected in MR signal intensity and images (Figure 4).

As for visualizing the sol and gel states, the contrast between sol **3/4** and gel **1** + **3/4** is not as stark as that between sol **3** and gel **1** + **3** in T_1-weighted images. Unlike gel **1** + **3**, gel **1** + **3/4** is not completely dark at all TI values. However, just like gel **1** + **3**, gel **1** + **3/4** is still completely dark at higher TE values.

Combining the imaging results at 5 and 1 m*M* overall Gd(III) concentration, the sol to gel transition is best visualized by T_2-weighted imaging at higher TE values with the sol producing a bright spot and the gel producing a dark spot.

Small-Angle X-Ray Scattering (SAXS)

MRI studies point to high local concentration of Gd(III)-chelate as a result of hydrogelation. Considering that these hydrogels are made of peptide nanofibers,[18] it is hardly surprising that gelation leads to inhomogeneous distribution of Gd(III) and thereby high local Gd(III) concentration. What is surprising is the extent of Gd(III) aggregation in gel **3** as the gel is completely dark in both T_1- and T_2-weighted images. One possibility is that Gd(III)-chelate further aggregates inside the peptide fibers, forming clusters. To investigate this possibility, we employed SAXS to compare the structure of gel **1** + **2** with that of gel **1** + **3**.

Both gels, **1** + **2** and **1** + **3**, form networks made of fibrils with high scattering intensity [$I(q)$] (Figure 5A). The co-assembly of the peptides results in long-range ordered structures with the X-ray scattering intensity reaching a plateau within 24 hr after mixing. Guinier plots of $lnqI(q)$ vs q^2 for the two gels after 24 hr show a distinctive roll-over at $q^2 < 2 \times 10^{-4}$ Å^{-2} (Figure 5B), which is characteristic of highly asymmetric particles with one dimension much larger than the other two.[31] Indirect Fourier transform of $I(q)$ to $P(r)$ (not shown) suggests that the length of the fibrils in both gels exceed the limits of precise measurement for our instrument,

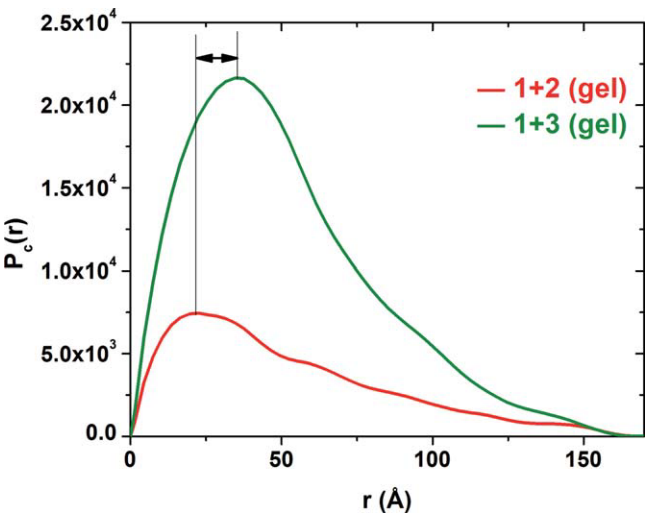

FIGURE 7 Pair-wise distance distribution functions [$P_c(r)$] obtained from 2D dummy atom model of the cross-sections of rod-like fibers in gel **1** + **2** (red) and gel **1** + **3** (green). Arrows mark the shift in the prevailing vector lengths.

Table II Structural Parameters of Oligopeptide Hydrogels Derived from Two-Dimensional Analysis of SAXS Data[a]

Gel	D_c (Å)	S_c (Å^2)	R_c (Å)	χ^2
1 + 2	170	3762	44.3	0.81
1 + 3	170	6309	41.7	0.79

[a] D_c is the maximum dimension of the peptide fiber cross-section in Å; S_c is the area of the peptide fiber cross-section in Å^2; R_c is the radius of gyration of the peptide fiber cross-section in Å; χ^2 reflects the quality of fit between the model and experimental data ($\chi^2 < 1$ indicates excellent fit).

which are limited to a minimum measurable q value of 0.008 Å^{-1}, corresponding to a maximum length scale of 400 Å ($d_{max} < \pi/q_{min}$; d_{max}–400 Å).[34] Therefore, we turned to the analysis of fiber cross-section in these two gels.

The two-dimensional analysis used a 2D dummy atom modeling approach that provides the representative shape of the cross-sections of the fibers underlying the hydrogel network (Figure 6) and the associated $P_c(r)$ functions (Figure 7). From $P_c(r)$, the maximum dimension of fiber cross-section, D_c, the area of fiber cross-section, S_c, and the radius of gyration of fiber cross-section, R_c, can be calculated (Table II).[32] The fibers in both gels have identical D_c values. Nonetheless, fibers in gel **1 + 3** are thicker than fibers in gel **1 + 2** (60 Å vs. 45 Å). One might have expected thicker fibers would lead to higher S_c and R_c values. However, S_c and R_c show the opposite trend of variation among the two hydrogels: while S_c increases from gel **1 + 2** to gel **1 + 3** (nearly two-fold), R_c decreases from gel **1 + 2** to gel **1 + 3** by almost 3 Å. R_c is the root mean square contrast-weighted distance of area elements from the center of scattering density, where the contrast is the difference in electron density between the scattering particle and the solvent. The smaller R_c value for the larger cross-sectional area of gel **1 + 3** thus implies that the electron dense Gd(III) is on average located more toward the center of the cross sectional area. It therefore appears that the incorporation of Gd(III)-chelate leads to thicker fibers with Gd(III)-chelate clustered toward the center of fiber cross-section. This further clustering of Gd(III)-chelates within peptide fibers provides an explanation as to why the MR signal is completely saturated in gel **1 + 3**.

CONCLUSION

In the absence of Gd(III)-chelate, gelation of the oligopeptide pair has little effect on MR signal intensity. In the presence of covalently linked Gd(III)-chelate, gelation of the oligopeptide pair produces significant change in water relaxation and MR signal intensity. At 5 mM overall Gd(III) concentration, gelation results in complete signal saturation and thereby dark spots in both T_1 and T_2-weighed images. At 1 mM overall Gd(III) concentration, gelation has much stronger effect on T_2 relaxation than on T_1 relaxation. The MRI results point to local enrichment of Gd(III)-chelate, which has two contributing processes: first, the aggregation of oligopeptides into fibers; second, within the peptide fibers, Gd(III)-chelate further aggregate into clusters, as indicated by SAXS studies. In the presence of covalently bound Gd(III)-chelate, there is s sharp contrast between the sol and gel states of peptide hydrogels.

REFERENCES

1. Caravan, P.; Ellison, J. J.; McMurry, T. J.; Lauffer, R. B. Chem Rev 1999, 99, 2293–22352.
2. De Leon-Rodriguez, L. M.; Lubag, A. J. M.; Malloy, C. R.; Martinez, G. V.; Gillies, R. J.; Sherry, A. D. Acc Chem Res 2009, 42, 948–957.
3. Marcos, M.; Cano, P.; Fantazzini, P.; Garavaglia, C.; Gomez, S.; Garrido, L. Magn Reson Imaging 2006, 24, 89–95.
4. Saldenha, K. J.; Doan, R. P.; Ainslie, K. M.; Desai, T. A.; Majumdar, S. Magn Reson Imaging 2011, 29, 40–49.
5. Taylor, C.; Carballido-Gamio, J.; Majumdar, S.; Li, X. Magn Reson Imaging 2009, 27, 779–784.
6. Plank, C. M.; Kubin, K.; Weber, M.; Marlovits, S.; Trattnig, S. C. Magn Reson Imaging 2005, 23, 739–744.
7. Burstein, D.; Velyvis, J.; Scott, K. T.; Stock, K. W.; Kim, Y. J.; Jaramillo, D.; Boutin, R. D.; Gray, M. L. Magn Reson Imaging 2001, 45, 36–41.
8. Brasch, R. C. Magn Reson Med 1991, 22, 282–287.
9. Bul,l S. R.; Guler, M. O.; Bras, R. E.; Venkatasubramanian, P. N.; Stupp, S. I.; Meade, T. J. Bioconjug Chem 2005, 16, 1343–1348.
10. Karfield, L. S.; Bull, S. R.; Davis, N. E.; Meade, T. J.; Barron, A. E. Bioconjug Chem 2007, 18, 1697–1700.
11. Toth, E.; Helm, L.; Kellar, K. E.; Merbach, A. E. Chem Eur J 1999, 5, 1202–1211.
12. Karfield-Sulzer, L. S.; Waters, E. A.; Davis, N. E.; Meade, T. J.; Barron, A. E. Biomacromolecules 2010, 11, 1429–1436.
13. Manus, L. M.; Mastarone, D. J.; Waters, E. A.; Zhang, X. Q.; Schultz-Sikma, E. A.; MacRenaris, K. W.; Ho, D.; Meade, T. J. Nano Lett 2010, 10, 484–489.
14. Wiener, E. C.; Brechbiel, M. W.; Brothers, B.; Magin, R. L.; Gansow, O. A.; Tomalia, D. A.; Lauterbur, P. C. Magn Reson Med 1994, 31, 1–8.
15. Toth, E.; Pubanz, D.; Vauthey, S.; Helm, L.; Merbach, A. E. Chem Eur J 1996, 2, 1607–1615.
16. Modo, M.; Mellowdew, K.; Cash, D.; Fraser, S. E.; Meade, T. J.; Williams, S. C. Neuroimage 2004, 21, 311–317.
17. McDonald, M. A.; Watkin, K. L. Acad Radiol 2006, 13, 421–427.
18. Ramachandran, S.; Tseng, Y.; Yu, Y. B. Biomacromolecules 2005, 6, 1316–1321.
19. Ramachandran, S.; Trewhella, J.; Tseng, Y.; Yu, Y. B. Chem Mater 2006, 18, 6157–6162.
20. Martinez, J.; Laur, J. Synthesis 1982, 11, 979–981.
21. Chan, W. C.; White, P. D. Fmoc Solid Phase Peptide Synthesis: A Practical Approach; OxfordUniversity Press: New York, 2000; p 1–75.

22. Bodanszky, M.; Bodanszky, A. The Practice of Peptide Synthesis; Springer-Verlag: Berlin, 1994. p 21–22.
23. Gill, S. C.; von Hippel, P. H. Anal Biochem 1989, 182, 319–326.
24. Rorden, C.; Brett, M. Behav Neurol 2000, 12, 191–200.
25. Smith R. C.; Reinhold C.; McCauley, T. R.; Lange, R. C.; Constable, R. T.; Kier, R.; McCarthy, S. Radiology 1992, 184, 671–675.
26. Hennig, J.; Naureth, A.; Friedburg, H. Magn Reson Med 1986, 3, 823–833.
27. Heidorn, D. B.; Trewhella, J. Biochemistry 1988, 27, 909–915.
28. Svergun, D. I.; Semenyuk, A. V.; Feigin, L. A. Acta Crystallogr 1988, A44, 244–250.
29. Svergun, D. I. J Appl Crystallogr 1991, 24, 485–492.
30. Svergun, D. I. J Appl Crystallogr 1992, 25, 495–503.
31. Guinier, A. Ann Phys (Paris) 1939, 12, 161–236.
32. Whitten, A. E.; Jeffries, C. M.; Harris, S. P.; Trewhella, J. Proc Natl Acad Sci USA 2008, 105, 18360–18365.
33. Svergun, D. I. Biophys J 1999, 76, 2879–2886.
34. Glatter, O.; Kratky, O., Eds. Small Angle X-Ray Scattering; Academic Press; London, 1982.